PHYSICAL REVIEW E **98**, 052201 (2018)

Resonant localized modes in electrical lattices with second-neighbor coupling

Xuan-Lin Chen,[1,2] Saidou Abdoulkary,[3] P. G. Kevrekidis,[4] and L. Q. English[1]
[1]*Department of Physics and Astronomy, Dickinson College, Carlisle, Pennsylvania 17013, USA*
[2]*Physics Department, Harbin Institute of Technology, Harbin 150001, Heilongjiang Province, China*
[3]*Département des Sciences Fondamentales, Faculté des Mines et des Industries Pétrolières, P.O. Box 46, Maroua, Cameroon*
[4]*Department of Mathematics and Statistics, University of Massachusetts, Amherst, Massachusetts 01003, USA*

(Received 19 June 2018; published 5 November 2018)

We demonstrate experimentally and corroborate numerically that an electrical lattice with nearest-neighbor and second-neighbor coupling can simultaneously support long-lived coherent structures in the form of both standard intrinsic localized modes (ILMs) as well as resonant ILMs. In the latter case, the wings of the ILM exhibit oscillations due to resonance with a plane-wave mode of the same frequency. This kind of localized mode has also been termed a nanopteron. Here we show experimentally and using realistic simulations of the system that the nanopteron can be stabilized via both direct and subharmonic driving. In the case of excitations at the zone center (i.e., at wave number $k = 0$), we observed stable ILMs as well as a periodic localization pattern in certain driving regimes. In the zone boundary case (of wave number $k = \pi/a$, where a is the lattice spacing), the ILMs are always resonant with a plane-wave mode, but they can nevertheless be stabilized by direct (staggered) and subharmonic driving.

DOI: 10.1103/PhysRevE.98.052201

I. INTRODUCTION

Intrinsic localized modes (ILMs), also known as discrete breathers (DBs), have been studied in a great variety of physical systems whose only requirements are that they (i) be spatially discrete and (typically) periodic, and (ii) exhibit nonlinearity [1,2]. These DB waveforms are exact time-periodic modes in (chiefly homogeneous) lattices for which the energy is spatially localized, typically over a few lattice sites. While some of the prototypical early studies arose in the context of vibrational-energy localization in atomic lattices [3,4], relevant considerations quickly expanded—involving also experimental work—to spin chains [5], and later to fabricated photonic lattices, Bose-Einstein condensates, Josephson-junction arrays, and microelectromechanical systems (MEMS), to name just a few examples [6–9]. More recently, materials systems such as granular chains [10–12] as well as electrical lattices [13–15] have attracted some interest as media supporting self-localized modes.

One thing that was realized early on was that ILMs could only exist when their frequencies fell outside of the spectrum of linear, extended-wave modes. In fact, even the overtones of the ILM were forbidden to overlap with any plane-wave mode frequency. This was established rigorously for Hamiltonian lattices [16,17]. On the other hand, it was also demonstrated that discrete breatherlike modes could exist in certain circumstances even when they did intersect part of the linear dispersion curve. In these cases, the mode energy was the highest in a very narrow central region of space, but it did not strictly go to zero with distance from that center. Instead, the tails of the ILM were found to exhibit small spatial oscillations consistent with the wave number of the resonant plane-wave mode. This type of phenomenon was reported, for instance, in numerical studies of spin-wave localization in spin chains with second-neighbor Heisenberg interactions [18–21]. The authors named this type of self-localization an “intrinsic localized spin-wave resonance.” No corresponding experimental observations were obtained, to the best of our knowledge, in this setting. The term *nanopteron* has also been used to signify a solitonlike solution featuring a small oscillatory background, and additionally discrete versions of such a solitary wave have been discussed [22,23]; such structures are also referred to as “weakly nonlocal solitary waves,” and a summary of (early) theoretical and numerical efforts along this direction was given in Ref. [24]. However, experimental studies of such excitations remain very limited; the only systematic example that we are aware of concerns the propagation of weakly nonlocal traveling waves in a woodpile lattice in the work of Ref. [25]. Coherent structures in the form of weakly localized discrete breathers will be a focal point of the present study. These are resonant in the sense that their frequency does intersect the linear dispersion curve, which means that some energy transfer between a plane-wave mode and the ILM can occur.

Another key feature of the present work is the consideration of beyond nearest-neighbor interactions, through the inclusion of second neighbors. The importance of incorporating such interactions when studying energy localization has also been reported in a variety of other discrete extended systems, many of which can be modeled by the nonlinear Schrödinger equation [26–28]. A particular proposal of this type, through consideration of so-called zigzag lattices in nonlinear optics [29], subsequently found remarkable experimental realizations in the context of femtosecond laser-written waveguide arrays [30]. Subsequent studies in that context went beyond the study of localization and also toward the observation of (anharmonic) Bloch oscillations by employing zigzag waveguide arrays in which the second-neighbor coupling could be controllably tuned [31]. The relevant

2470-0045/2018/98(5)/052201(9)

phenomenology has remained an active topic of study in recent investigations [32,33], and it will also be central to the discrete breather phenomenology in the electrical lattices presented herein.

In this paper, we report on experimental and numerical observations of ILMs in an electrical lattice with nearest-neighbor and second-neighbor coupling. A key distinguishing feature of our work with respect to earlier optical realizations is that contrary to the scenarios of the latter type [30,31], where the second-neighbor coupling is predominantly linear, in our case it is fundamentally nonlinear, as will be evident in the mathematical model below. Moreover, the theoretical model contains a nonlinear coupling of each node to its nearest neighbors comparable to the on-site nonlinearity, a feature also rather uncommon in the optical setting; see, e.g., the relevant discussion of [34]. It is shown that this lattice can support two types of long-lived, experimentally observable localized modes: the standard ILM (whose wings asymptotically approach zero), and the resonant ILM or nanopteron (whose wings manifest oscillations). The former branches off from the zone-center (ZC) mode ($k = 0$), whereas the latter derives from the zone-boundary (ZB) mode ($k = \pi/a$). For a first analytical exploration, we deploy a simplified model of the lattice that uses harmonic and square-anharmonic on-site terms, approximating the full nonlinearity of the electrical unit-cell resonator fairly well while ignoring the resistive currents through the diode. In this context, we can numerically approximate the solutions, and we show that both standard ILMs as well as resonant ILMs come in two varieties of double-peaked and single-peaked profiles.

On the experimental side, both types of localized modes are generated and stabilized with an external driver. In the case of the standard ILM (here also referred to as the ZC ILM), the driving signal is spatially homogeneous with a frequency just below the bottom of the linear dispersion curve. For resonant ILMs or nanopterons (also referred to as ZB ILMs), we employ a spatially staggered driver just below the ZB mode in frequency, as well as subharmonic driving. Realistic dynamical simulations are performed, and these too indicate that such excitations can be generated via modulational instability of the relevant extended mode.

II. THE SYSTEM AND THE THEORETICAL MODEL

The nonlinear lattice shown in Fig. 1 consists of N unit cells each comprised of a linear inductor L_1 in parallel with a nonlinear capacitor $C(V)$ and coupled via inductances L_2 and L_3. The nonlinear capacitor is typically realized by a (reverse-biased) varactor diode with a capacitance given as a function of the differential voltage V_n across the capacitor. More details about the diode are given in panel (b) of Fig. 1.

For reasons of analytical tractability, we begin the discussion by exploring a simplified dynamical model, where the nonlinear element is considered to be strictly capacitive, which, in contrast to a diode, precludes the possibility of resistive currents flowing through the element. This is the primary limitation of this model in modeling the real varactor diode used in the experiment. Later, we will come back to a more realistic, yet also more complex, model that we use as the basis for direct simulations. This more complex model is based on the elements shown in Fig. 1(b).

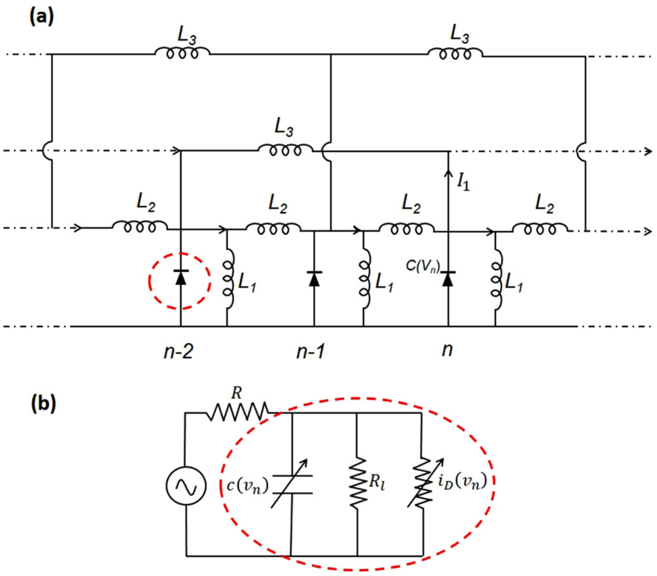

FIG. 1. (a) Schematic representation of the coupled nonlinear transmission line. (b) A closer view of the detailed diode model and the forcing by an external signal.

Proceeding with the simpler model, and using the Kirchhoff node rule, the equations for the unit-cell circuit become

$$\begin{aligned} I_n &= I_{n+1} + I_1 + \frac{dQ_n}{dt} + I_{L1}, \\ L_3 \frac{dI_1}{dt} &= 2V_n - V_{n-2} - V_{n+2}, \end{aligned} \tag{1}$$

where I_{L_1} is the current through the inductor L_1, and Q_n is the charge on the nth capacitor. Combining Eq. (1) with the auxiliary equations $L_1 dI_{L_1}/dt = V_n$ and $L_2 dI_n/dt = V_{n-1} - V_n$, we obtain the following governing equation:

$$\begin{aligned} \frac{d^2 Q_n}{dt^2} &= -\frac{V_n}{L_1} + \frac{1}{L_2}(V_{n+1} + V_{n-1} - 2V_n) \\ &\quad + \frac{1}{L_3}(V_{n+2} + V_{n-2} - 2V_n). \end{aligned} \tag{2}$$

To get the relationship between Q_n and V_n, a particular functional form of $C(V)$ has to be specified, which can then be integrated with respect to the voltage to yield $Q(V)$. For instance, if an exponential dependence is assumed, $C(V_n) = C_0 \exp(-\alpha V_n)$, then integration and subsequent inversion of the resulting expression will produce,

$$V_n = -\frac{Q_0}{C_0} \ln\left(1 - \frac{Q_n}{Q_0}\right), \tag{3}$$

where $Q_0 = C_0/\alpha$. However, this frequently used (due to its simplicity) relationship when applied to a single oscillator does not generate a soft nonlinearity. In other words, contrary to what is the case for the latter, here the mode frequency increases with increasing amplitude. It is an experimental fact about the varactor diodes that they are characterized by soft nonlinearity. Even truncating the Taylor expansion of Eq. (3) after the cubic term would still yield an oscillator whose frequency increases with amplitude. To achieve soft nonlinearity, we focus on the scenario in which the square term dominates over the cubic (see also Ref. [13]). It turns out that keeping only the first two terms provides a frequency-amplitude dependence that is fairly close to the experimental data. This approximation was also used in Ref. [35]. Thus, we assume

$$V_n = \frac{Q_0}{C_0}\left(q_n + \frac{1}{2}q_n^2\right), \tag{4}$$

with $q_n = Q_n/Q_0$ [Eq. (3)].

Now inserting Eq. (4) into Eq. (2), we obtain

$$\begin{aligned}\frac{d^2q_n}{d\tau^2} = &-\left(q_n + \frac{1}{2}q_n^2\right) + \gamma\left[\left(q_{n+1} + \frac{1}{2}q_{n+1}^2\right)\right.\\ &\left.+\left(q_{n-1} + \frac{1}{2}q_{n-1}^2\right) - 2\left(q_n + \frac{1}{2}q_n^2\right)\right]\\ &+\delta\left[\left(q_{n+2} + \frac{1}{2}q_{n+2}^2\right) + \left(q_{n-2} + \frac{1}{2}q_{n-2}^2\right)\right.\\ &\left.-2\left(q_n + \frac{1}{2}q_n^2\right)\right],\end{aligned} \tag{5}$$

where $\tau = \omega_0 t$ is the effective time parameter, $\omega_0^2 = 1/(L_1C_0)$ is the frequency of the uniform mode, and $\gamma = L_1/L_2$ and $\delta = L_1/L_3$ are inductor ratio parameters.

Anticipating the possibility of dynamic anharmonic modes, we set a trial solution [36] as

$$q_n(\tau) = A[\phi_n(\tau)\cos(kna + \tilde{\omega}\tau) + \xi_n(\tau)], \tag{6}$$

where A is the maximum amplitude, a is the lattice spacing, $\cos(kna + \tilde{\omega}\tau)$ is a moving carrier wave with $\tilde{\omega} = \omega/\omega_0$, while k and ω are its wave vector and frequency, respectively. $\phi_n(\tau)$ and $\xi_n(\tau)$ are the vibrational envelope and the nonoscillatory displacement, respectively. For initial displacements, $\tau = 0$, $\phi_n\cos(kna)$ is often known as ac displacement, and ξ_n as dc displacement. We set $A = 1$ for simplicity, then insert Eq. (6) into Eq. (5), and use the rotating-wave approximation method (RWA), which discards the terms oscillating at multiples of the fundamental mode frequency. Also assuming that ϕ_n and ξ_n are τ-independent, we can obtain the cosine terms

$$\begin{aligned}&\phi_n[-1 + \tilde{\omega}^2 - 2\delta - 2\gamma - (1 + 2\delta + 2\gamma)\xi_n]\\ &\quad+\gamma[\phi_{n-1}(1 + \xi_{n-1}) + \phi_{n+1}(1 + \xi_{n+1})]\cos(ak)\\ &\quad+\delta[\phi_{n-2}(1 + \xi_{n-2}) + \phi_{n+2}(1 + \xi_{n+2})]\cos(2ak) = 0,\end{aligned} \tag{7}$$

and the static displacement terms

$$\begin{aligned}&\delta\phi_{n-2}^2 + \gamma\phi_{n-1}^2 - \phi_n^2 - 2(\delta + \gamma)\phi_n^2 + \gamma\phi_{n+1}^2\\ &\quad+4\gamma\xi_{n-1} + 2\gamma\xi_{n-1}^2 + \delta\big[\phi_{n+2}^2 + 2\xi_{n-2}(2 + \xi_{n-2}) - 8\xi_n\big]\\ &\quad-4\xi_n - 8\gamma\xi_n - 2\xi_n^2 - 4\delta\xi_n^2 - 4\gamma\xi_n^2 + 4\gamma\xi_{n+1}\\ &\quad+2\gamma\xi_{n+1}^2 + 4\delta\xi_{n+2} + 2\delta\xi_{n+2}^2 = 0.\end{aligned} \tag{8}$$

Equations (7) and (8) are used in the next section to find numerically *approximate* breather solutions that can be tested against the experimental and numerical results.

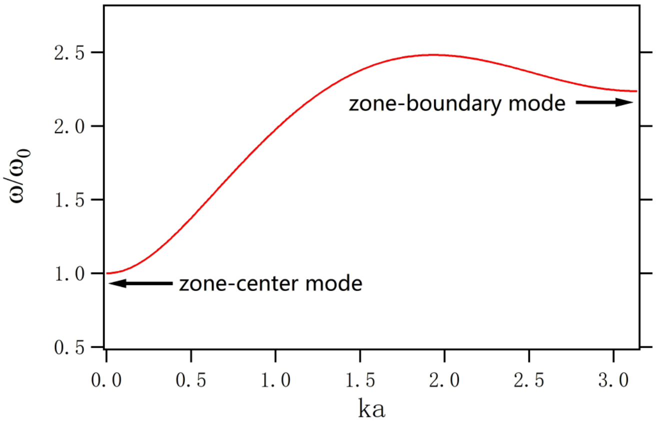

FIG. 2. Dispersion relation showing frequency as a function of ka. The standard ILMs and resonant ILMs should be found at $ka = 0$ and $ka = \pi$ under the dispersion curve, respectively.

The linearized (around the vanishing state) form of Eq. (5) yields the following dispersion relation:

$$\tilde{\omega}^2(k) = 1 + 4\gamma\sin^2\left(\frac{ka}{2}\right) + 4\delta\sin^2(ka). \tag{9}$$

The dispersion curve is shown in Fig. 2. A frequency gap exists below the zone-center (uniform) mode due to the inductor to ground in each unit cell, but additionally a quasigap also appears at the zone boundary due to the second-neighbor inductors. By this term (quasigap) we mean the absence of plane-wave modes below the ZB mode in frequencies that have a wave number close to π/a (i.e., close to the edge of the Brillouin zone). This creates the possibility that resonant ILMs could be found arising from the ZB mode. Note that the curvatures of the band at the two zone edges are both positive (for $\delta > 0$).

The analysis above was based on a simplified model of the varactor diode as a nonlinear capacitor. A fuller description of the diode must also account for current going through it, thereby including resistive dissipation. Reference [37] derives equations that include this feature as well as external driving, which, when modified to our system with second-neighbor coupling, read

$$\begin{aligned}c(v_n)\frac{dv_n}{d\tau} &= y_n - i_D(v_n) + \frac{\cos(\Omega\tau)}{RC_0\omega_0}\\ &\quad-\left(\frac{1}{R_l} + \frac{1}{R}\right)\frac{v_n}{\omega_0C_0},\\ \frac{dy_n}{d\tau} &= -v_n + \frac{L_1}{L_2}(v_{n+1} + v_{n-1} - 2v_n)\\ &\quad+\frac{L_1}{L_3}(v_{n+2} + v_{n-2} - 2v_n),\end{aligned} \tag{10}$$

where R is the driving resistor of 10 kΩ, y_n represents the current through the inductor L_1, and R_l, $c(v)$, and $i_D(v)$ are given in Ref. [37] as

$$i_D(v) = -\frac{I_s}{\omega_0C_0V_d}\exp(-\beta V_d v),$$

with $\beta = 38.8\text{V}^{-1}$ and $I_s = 1.25 \times 10^{-14}$ A. Furthermore, $v = \frac{V}{V_d}$, $c = \frac{C}{C_0}$, and

$$C(V) = \begin{cases} C_v + C_w(V') + C(V')^2 & \text{if} \quad V \leqslant V_c, \\ C_0 e^{-\alpha V} & \text{if} \quad V > V_c. \end{cases}$$

Here, $V' = (V - V_c)$, $\alpha = 0.456\text{V}^{-1}$, $C_v = C_0 \exp(-\alpha V_c)$, $C_w = -\alpha C_v$, $C = 100\,\text{nF/V}^2$, and $V_c = -0.28$ V. It is worthwhile to note that the presence of (and division by) $c(v_n)$ renders all the terms (including the second-neighbor ones) in Eq. (10) nonlinear if we attempt to derive a second-order equation, say for y_n.

Equation (10) represents the more accurate variant of our model that we will use to compare more directly to experimental results [37]. Importantly, it encompasses the driving and damping aspects inherent in the electrical lattice. Hence, we utilize in what follows the simplified model of Eq. (5) to obtain insight into the potential existence and structural form of the breathers; then we explore whether such structures survive in the more realistic setting containing the driving and damping.

III. RESULTS AND DISCUSSION

A. Approximate (RWA-based) numerical solutions in the undriven, undamped lattice

We now employ the Newton-Raphson method to determine the solutions of Eqs. (7) and (8). If an initial guess of displacements that are single-humped and localized at the center of the lattice is given, then solutions to these coupled, nonlinear algebraic equations can be determined though an iterative process. Here, motivated by the experiments below, we use the values $L_1 = L_2 = 470\,\mu\text{H}$, $L_3 = 680\,\mu\text{H}$, so $\gamma = 1$, $\delta \approx 0.7$. Both ZB ($ka = \pi$) and ZC ($ka = 0$) ILMs are found in chains with 35 sites when imposing periodic boundary conditions, as shown in Fig. 3. Notice that the dc value is close to zero except near the ILM centers.

The relationship between the frequency of ILMs and their ac amplitude is shown in Fig. 4, which was obtained via continuation of the solution in ω. The frequencies of single-peaked ILMs are always a little higher than those of double-peaked ILMs with the same ac amplitude. What is interesting is that for smaller lattices, here $N = 35$, the ILM branches off from the $k = 0$ plane-wave (uniform) mode at a nonzero amplitude. For larger lattice sizes, this does not occur, as is shown in the figure for $N = 128$. The qualitative reason is that for small lattices, the zone-center ILM is wide enough that its wings do not reach a small amplitude within the extent of the lattice.

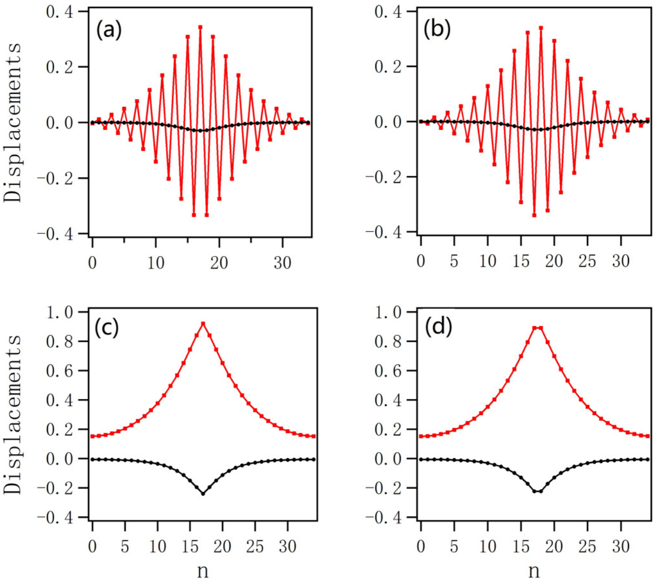

FIG. 3. Comparison of ac and dc displacements for *approximate* ILMs, as obtained within the RWA from the solution of Eqs. (7) and (8). (a) Single-peaked ZB (resonant) ILM ($\tilde{\omega} = 2.22$), (b) double-peaked ZB ILM ($\tilde{\omega} = 2.22$), (c) single-peaked ZC ILM ($\tilde{\omega} = 0.95$), and (d) double-peaked ZC ILM ($\tilde{\omega} = 0.95$). The filled squares (red) are for ac displacements, and the filled circles (black) show the dc displacements.

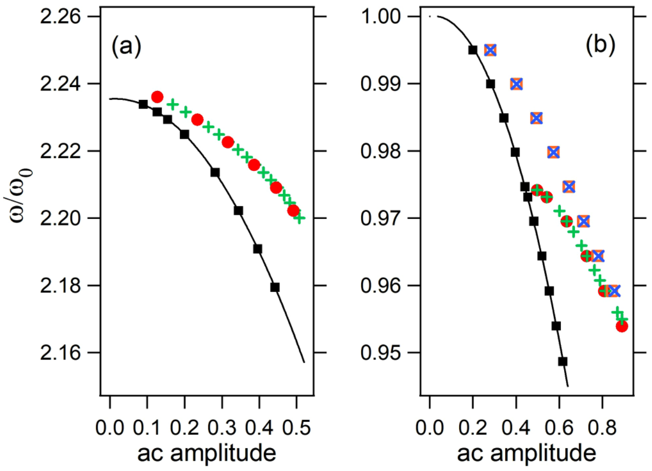

FIG. 4. The frequency of ILMs and associated plane-wave modes as a function of ac amplitude, $\phi_n \cos(kna)$, of the ILM center. (a) Zone-boundary ILMs and (b) zone-center ILMs. The filled squares (black) are for $ka = 0$ and $ka = \pi$ plane-wave modes, respectively, which also have parabolic fitting lines (black). For $N = 35$, the filled circles (red) are for double-peaked modes, and the plus markers (green) show the single-peaked modes. A second lattice size, $N = 128$ (squares and crosses), is also shown; here the ILMs are seen to branch off sooner.

When the frequency of the single-peaked ZB ILM becomes lower, and its amplitude higher, a strong resonance appears between our approximate breather profiles, as obtained by Eqs. (7) and (8) and shown in Fig. 5(a), and the resonant linear plane-wave mode of the dispersion curve. Figure 5(b) shows the numerical evolution using the RWA output as an initial condition. This waveform does not appear to be robust when simulated using the full governing equations. The time evolution of Eq. (5) using a Runge-Kutta algorithm is shown in Fig. 5(b). We see that the initial waveform propagates for a number of periods, but eventually disintegrates by radiating energy into the resonant extended modes. This is also clearly seen in the two-dimensional Fourier transform graphs. Figure 5(c) corresponds to the early times (from 0 to 30 on the τ axis, before full disintegration), while Fig. 5(d) shows

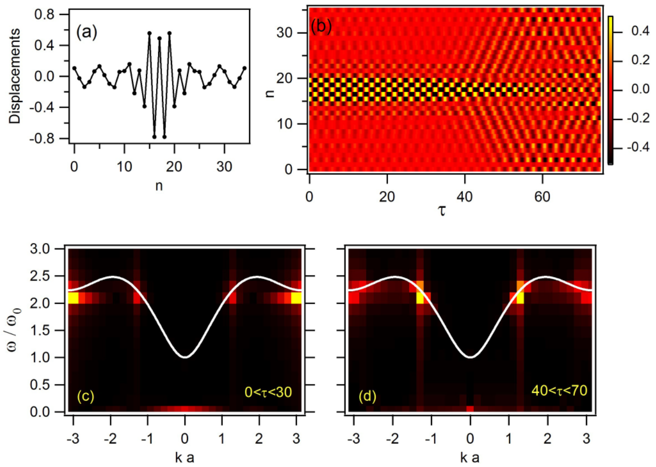

FIG. 5. (a) Displacements of a single-peaked resonant ILM ($\tilde{\omega} = 2.14$); (b) time evolution of the single-peaked resonant ILM at $\tilde{\omega} = 2.14$; (c) Fourier transformation of the time evolution during $0 < \tau < 30$ and (d) during $40 < \tau < 70$, compared with the dispersion curve (white line).

the later time window (between 40 and 70 on the τ axis). Comparing these two images, we see clearly that energy is transferred from the ZB ILM to the resonant extended mode. In this way, the approximate as well as resonant nature of the relevant ZB waveform is manifested. For smaller amplitude ILMs, this transfer also happens, but at a slower rate, so that they appear robust for longer periods of time. At the ZC, while the ILM has no direct resonance, its overtones still intersect the linear spectrum. The RWA cannot account for this process, but direct simulations also indicate a slow decay of the long-lived localized mode.

B. Experimental results and numerical simulations

We have constructed the lattice shown in Fig. 1 of 32 nodes with $L_1 = 470\ \mu$H, $L_2 = 680\ \mu$H, and $C_0 = 800$ pF. Care was taken to select inductors with very similar inductances to reduce spatial inhomogeneity. These component values yield a frequency of $f_0 = \omega_0/(2\pi) \cong 260$ kHz. The lattice takes the shape of a ring to eliminate boundaries. This also practically implies the generic implementation of periodic boundary conditions in the context of numerical computations.

To access the area of interest in k space, we drive the system at all lattice nodes via 10 kΩ resistors connected to the top end of the diodes. The idea then is to directly excite plane-wave modes by having the driver match their frequency; alternatively, the driver can also be set to twice the mode frequency for subharmonic excitation—a method we employ later. For direct driving, we also have added some control of the driver wave number. In particular, in order to stimulate the ZB plane-wave mode, we tune the signal generator to about 580 kHz and introduce a phase shift of π between neighboring nodes. This kind of spatially staggered driving can be easily accomplished by sending the original sinusoidal driving signal through an inverter (such as an inverting amplifier of gain 1) for half of the nodes while using the direct signal for the other half.

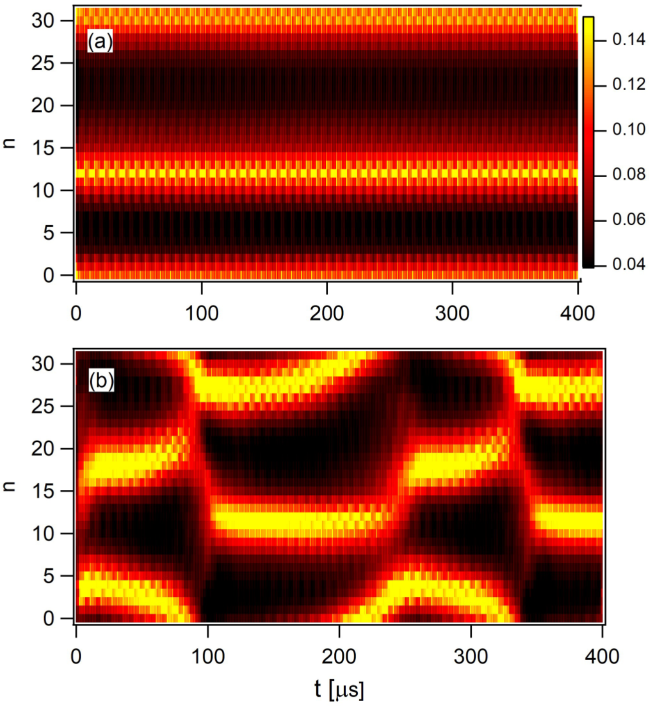

FIG. 6. Experimental data illustrating the averaged square voltage (v_n^2) evolution (color bar on the right) at each node n of the lattice as a function of time. (a) The spatially uniform driver was set to 249 kHz in frequency at an amplitude of 2.0 V. Two broad zone-center ILMs are generated. (b) The driver frequency is decreased to 239 kHz. The system develops a repeating pattern of two ILMs that interact multiple times.

Performing a frequency sweep with a spatially homogeneous driving, only the ZC uniform mode is observed, whereas for spatially staggered driving, as is natural to expect, we only couple to the ZB mode. Having demonstrated that the ZC and ZB extended modes can be excited in this fashion, we explore whether ILMs can also be generated and stabilized by these two types of driving. In particular, we examine experimentally whether a temporally periodic driver can couple to and sustain these modes.

Figure 6 shows that this is indeed the case for the zone center when driving uniformly at each node in the experiment. The averaged square voltage density plot (see the color bar) indicates that two fairly broad ILMs are generated—their width is enhanced by the presence of next-neighbor couplings. The average square of the voltage is shown at each node, which was calculated by squaring all voltages and then using a boxcar integration method with a time window of one period. The driver frequency here is set to 249 kHz, or $\omega_d = 0.97\omega_0$, and the amplitude is 2.0 V. When the driver frequency is decreased to 239 kHz, or $\omega_d = 0.93\omega_0$, a repeating pattern of two ILMs merging and splitting is observed.

Direct numerical simulations of Eq. (10) corroborate these experimental findings. Here, a lattice of 35 nodes is initiated with small spatial noise; the time evolution of its averaged square voltage in the presence of driving is shown in Fig. 7. In Fig. 7(a), we can see two ZC ILMs, and they seem quite robust at this driving frequency. When the frequency gets lower as

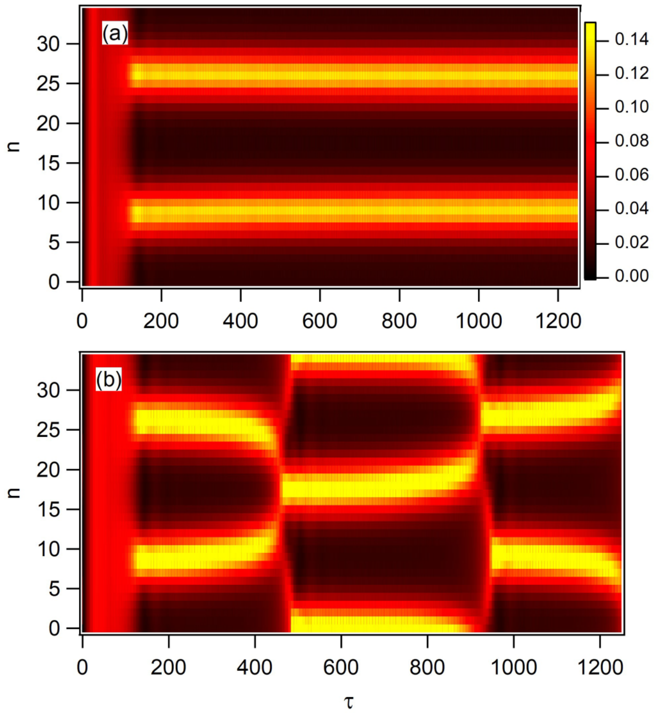

FIG. 7. The time-evolution numerical results of the averaged square voltage of ZC ILMs at an amplitude of 2.0 V with a frequency of (a) $\tilde{\omega} = 0.97$ and (b) $\tilde{\omega} = 0.93$.

shown in Fig. 7(b), the dynamics exhibits a periodic localization pattern, but otherwise persists. Thus, the simulations appear to faithfully reproduce the experimental observation of Fig. 6 at identical driving parameters. The qualitative reason for the appearance of the dynamic localization pattern at these lower frequencies is that it represents a transition region to one ILM at even lower frequencies.

Next, let us turn to the zone boundary, where we switch to spatially staggered driving ($k = \pi/a$). The linear ZB mode at $k = \pi/a$ is calculated to reside at around 585 kHz. Figure 8(a) shows the experimental results for a sinusoidal driver frequency set to 500 kHz, or $\omega_d = 0.85\omega_{\text{ZB}}$, and an amplitude of 1.6 V. Four ZB ILMs are observed in the lattice for these driving conditions.

Figure 8(b) shows the corresponding numerical simulation of the excited ZB ILMs. The driver amplitude is identical, although the frequency has to be raised somewhat, here to 539 kHz. The initial displacements start from zero but with a small noise perturbation. Four stable ZB ILMs are generated via modulational instability (MI). The MI is not shown in this figure. In Fig. 8(c), the ILMs centered at nodes 7 and 8 as well as 30 and 31 in the simulation are clearly identifiable as having single-peaked symmetry in the lowest panel. In the middle panel, after some elapsed time within the same period, the staggered driver signature dominates. Then, in the top panel, the two ILMs centered about 8 and 30 have clearly changed toward a double-peaked antisymmetric configuration. We point out that this periodic exchange between double-peaked and single-peaked ILM profiles continues thereafter, in accordance also with the experimental results of Fig. 8(a).

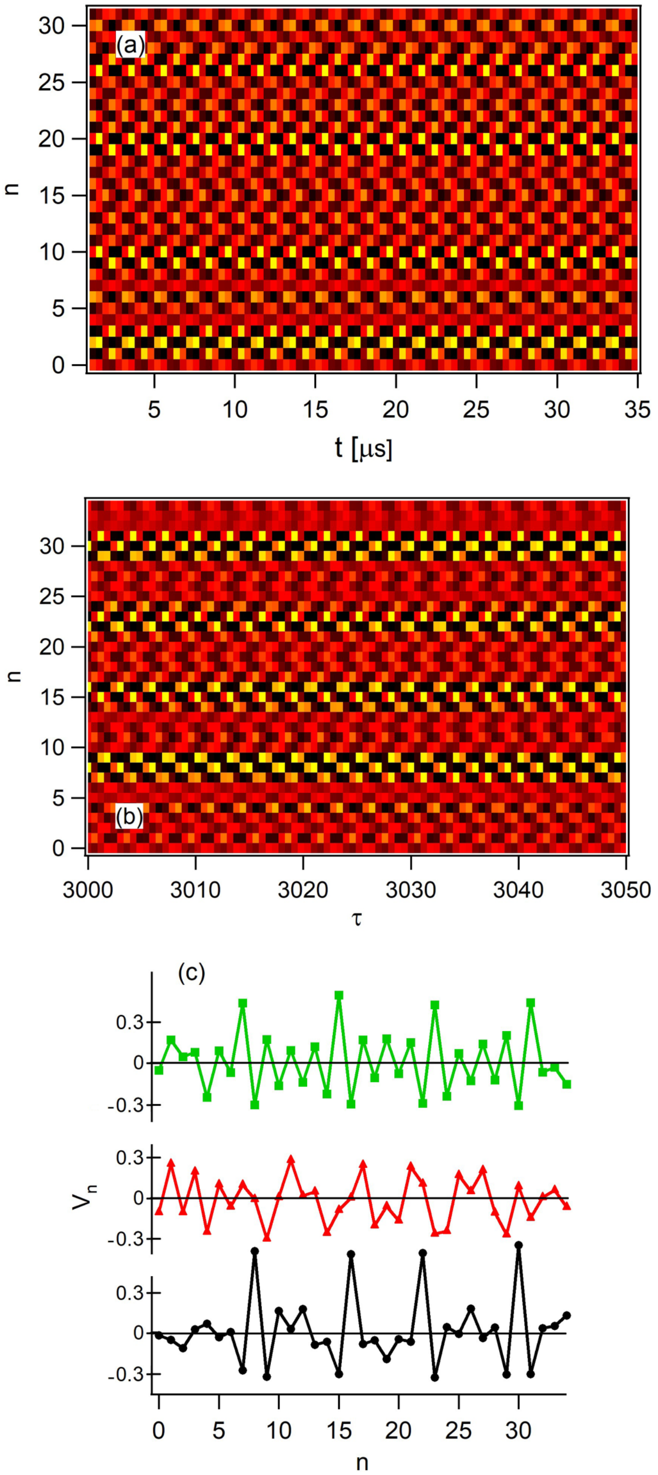

FIG. 8. (a) Experimental data for $f_d = 500$ kHz and an amplitude 1.6 V. We see multiple ZB ILMs. (b) Numerical simulation with the same driving voltage, and a frequency of $\omega = 539$ kHz. (c) Numerical voltage profile at three different times: $\tau = 3010$, 3011, and 3012.

In the experiment it is possible to lower the driver frequency further while increasing the amplitude in order to reduce the number of ZB ILMs. This is illustrated in Fig. 9(a), where only one ILM remains. From the experimental profiles

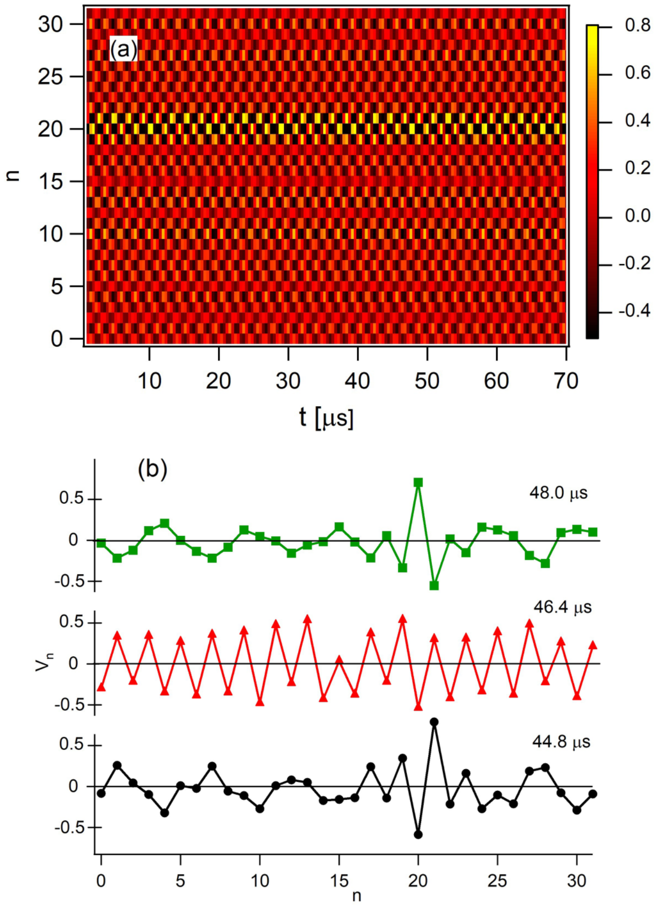

FIG. 9. (a) Experimental frequency is lowered to 479 kHz and amplitude raised to 2.0 V. We observe one ZB ILM persisting indefinitely. (b) Voltage profile at three times: $t = 44.8$, 46.4, and 48.0 μs. The resonance signature in the wings of the ILM is clearly evident in the bottom and top traces, but the ZB signature of the driver dominates in the middle trace.

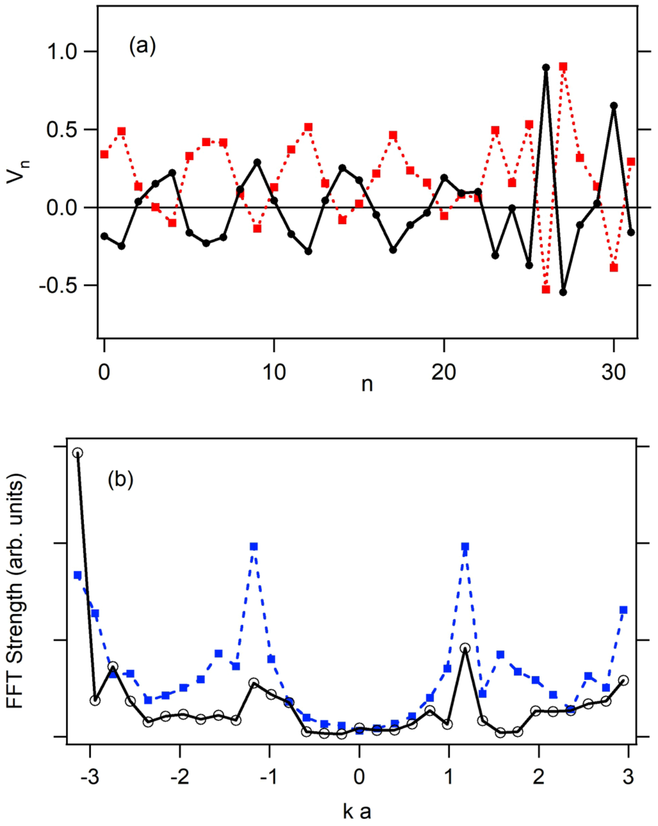

FIG. 10. (a) Experimental node voltages for subharmonic driving at a frequency of 980 kHz with an amplitude of 9.5 V. We observe one main resonant, subharmonically driven ILM, and voltage profiles at two instants of time: 42.8 (solid) and 43.6 (dotted) μs. (b) The spatial Fourier amplitudes computed from the experimental data. The dashed trace with square markers (blue) is computed from the dataset in (a). Circles (black) are obtained from the data in Fig. 9. We see that subharmonic generation of resonant ILMs enhances the oscillatory background.

displayed in Fig. 9(b), it is clear that this represents a ZB ILM with neighboring nodes out-of-phase with one another. Furthermore, the data display clear evidence for ILM resonance with the part of the plane-wave spectrum with which it shares the same frequency. This is again most easily discerned in Fig. 9(b), which shows the voltage profile at three particular instants of time. We see the ILM with a symmetric (top panel) and antisymmetric (bottom panel) configuration of the voltages, while the middle panel transitions between the two. Note also that the plane-wave signature is evident within the wings of the ILM in both the top and bottom panels, yet the nature of the configuration is less clear in the middle panel.

A spatially staggered driving signal can ordinarily lock onto any ZB mode, and here we find that it can also stabilize a resonant ILM. A question is whether such ILMs can also be excited via spatially uniform but subharmonic driving. It is known that subharmonic driving, being itself a nonlinear process, can project out into modes within the linear band, thus potentially coupling to a ZB ILM. Indeed, we find that the resonant ILM at the ZB can be excited in this manner. The results are shown in Fig. 10(a). Here the driver frequency was set to 980 kHz with a large amplitude of 9.5 V and was of square-wave shape. One main ILM centered at nodes 26 and 27 is generated (along with some smaller energy localization at $n = 30$). However, we now also see an enhanced plane-wave signature from the resonant part of the dispersion curve.

To analyze the difference between the two types of driving, we compute from the experimental data, $V(n, t)$, the two-dimensional fast Fourier transform, which yields a Fourier amplitude as a function of frequency and wave number. We then select the slice corresponding to the fixed oscillation frequency of the ILM. The result is displayed in Fig. 10(b), where the dashed blue line (square markers) corresponds to the subharmonic driver, and the solid black line (circles) corresponds to a direct driver. The latter is computed from the data in Fig. 9. It is clear that the peak response heights are distinct for the two types of driving. While direct driving results in the greatest amplitude at the ZB ($k = -\pi/a$), subharmonic driving deposits slightly more energy into the resonant plane waves than the ZB ILM. This may not be surprising since a subharmonic driver can presumably excite these modes directly and not just indirectly via the ILM resonance with these plane waves.

IV. CONCLUSIONS AND FUTURE WORK

We have demonstrated experimentally that two types of long-lived (enough to also be experimentally observed) ILMs exist and can be generated in an electrical lattice with the addition of second-neighbor couplings: standard and resonant ILMs, also known as nanopterons. The former appear at the ZC, whereas the latter appear at the ZB. We have furthermore investigated these ILMs numerically using a simplified model of the varactor diodes, and we identified suitable initial guesses for such breathers based on the undamped-undriven simplified model within the rotating-wave approximation.

In the experiment, resonant ILMs can be preserved over the course of the dynamical evolution by either direct or subharmonic driving. In the simplified model without gain and loss, the resonant ILM may scatter its energy into the resonant plane waves and be thus led to decay. However, more realistic numerical simulations that incorporate damping and driving show that resonant ILMs can be preserved at the ZB due to the action of the periodic driving. We conclude that at both the zone boundary as well as the zone center, ILMs can be found and stabilized by the driver, in good qualitative agreement with the RWA-predicted structures and the corresponding numerical simulations.

Nevertheless, numerous open questions have also emerged in this study. For the ZC modes, it does not elude us that their harmonics find themselves inside the band of linear excitations. Without dissipation, this would clearly represent a pathway that is detrimental to the longevity of these localized structures. The same is true for the ZB ILMs, which in the undamped and undriven model can, in principle, be resonantly decaying toward extended-state excitations. On the other hand, as indicated above, in the driven and damped model variant of the system, the breathers appear to be robust. Nevertheless, a natural question is whether they can constitute exact time-periodic solutions of the system, and perhaps even more importantly (from the relevant Floquet multiplier analysis of the corresponding monodromy matrix) whether they will be genuinely stable. A continuation over the frequencies may reveal possible variations and bifurcations along the relevant branch, potentially revealing the source of the observed mobility of the ZC structures, as the frequency is decreased. Numerous additional topics can be considered in further detail, including also the modulational stability in a semiexact analytical form: although this may not be possible to perform in the full breather setting, it should definitely be tractable in a monochromatic discrete nonlinear Schrödinger-like approximation of the model. A more systematic classification of the unstable modes and the corresponding byproducts of the MI may well prove helpful toward identifying the number of instability-induced breathers for each frequency. All these are important questions in this emerging field of the study of highly nonlinearly coupled chains involving both first and second neighbors. As such, they will be considered in future studies on the subject.

ACKNOWLEDGMENTS

P.G.K. acknowledges that this work was made possible by NPRP Grant No. 9-329-1-067 from Qatar National Research Fund (a member of Qatar Foundation). The findings achieved herein are solely the responsibility of the authors.

[1] D. K. Campbell, S. Flach, and Y. S. Kivshar, Phys. Today **57**(1), 43 (2004).
[2] S. Flach and A. Gorbach, Phys. Rep. **467**, 1 (2008).
[3] A. J. Sievers and S. Takeno, Phys. Rev. Lett. **61**, 970 (1988).
[4] J. B. Page, Phys. Rev. B **41**, 7835 (1990).
[5] R. Lai and A. J. Sievers, Phys. Rep. **314**, 147 (1999).
[6] J. W. Fleischer, M. Segev, N. K. Efremidis, and D. N. Christodoulides, Nature (London) **422**, 147 (2003).
[7] A. Smerzi, A. Trombettoni, P. G. Kevrekidis, and A. R. Bishop, Phys. Rev. Lett. **89**, 170402 (2002).
[8] E. Trías, J. J. Mazo, and T. P. Orlando, Phys. Rev. Lett. **84**, 741 (2000).
[9] M. Sato, B. E. Hubbard, and A. J. Sievers, Rev. Mod. Phys. **78**, 137 (2006).
[10] N. Boechler, G. Theocharis, S. Job, P. G. Kevrekidis, M. A. Porter, and C. Daraio, Phys. Rev. Lett. **104**, 244302 (2010).
[11] C. Chong, F. Li, J. Yang, M. O. Williams, I. G. Kevrekidis, P. G. Kevrekidis, and C. Daraio, Phys. Rev. E **89**, 032924 (2014).
[12] Y. Zhang, D. M. McFarland, and A. F. Vakakis, Granular Matter **19**, 59 (2017).
[13] M. Sato, S. Yasui, M. Kimura, T. Hikihara, and A. J. Sievers, Europhys. Lett. **80**, 30002 (2007).
[14] L. Q. English, R. B. Thakur, and R. Stearrett, Phys. Rev. E **77**, 066601 (2008).
[15] S. Shige, K. Miyasaka, W. Shi, Y. Soga, M. Sato, and A. J. Sievers, Europhys. Lett. **121**, 30003 (2018).
[16] R. S. MacKay and S. Aubry, Nonlinearity **7**, 1623 (1994).
[17] S. Flach, Phys. Rev. E **50**, 3134 (1994).
[18] R. Lai, S. A. Kiselev, and A. J. Sievers, Phys. Rev. B **56**, 5345 (1997).
[19] R. Lai and A. J. Sievers, Phys. Rev. B **55**, R11937(R) (1997).
[20] S. A. Kiselev, R. Lai, and A. J. Sievers, Phys. Rev. B **57**, 3402 (1998).
[21] G. Huang, S. Zhang, and B. Hu, Phys. Rev. B **58**, 9194 (1998).
[22] A. V. Savin, Y. Zolotaryuk, and J. C. Eilbeck, Physica D **138**, 267 (2000).
[23] G. Iooss and G. James, Chaos **15**, 015113 (2005).
[24] J. Boyd, *Weakly Nonlocal Solitary Waves and Beyond-All-Orders Asymptotics* (Kluwer, Amsterdam, 1998).
[25] E. Kim, F. Li, C. Chong, G. Theocharis, J. Yang, and P. G. Kevrekidis, Phys. Rev. Lett. **114**, 118002 (2015)
[26] P. G. Kevrekidis, B. A. Malomed, A. Saxena, A. R. Bishop, and D. J. Frantzeskakis, Physica D **183**, 87 (2003).
[27] B. Tang and K. Deng, Nonlin. Dyn. **88**, 2417 (2017).
[28] Y. B. Yao, D. J. Li, and B. Tang, Int. J. Mod. Phys. B **29**, 1550214 (2015).
[29] N. K. Efremidis and D. N. Christodoulides, Phys. Rev. E **65**, 056607 (2002).
[30] A. Szameit, R. Keil, F. Dreisow, M. Heinrich, T. Pertsch, S. Nolte, and A. Tünnermann, Opt. Lett. **34**, 2838 (2009).

[31] F. Dreisow, G. Wang, M. Heinrich, R. Keil, A. Tünnermann, S. Nolte, and A. Szameit, Opt. Lett. **36**, 3963 (2011).

[32] P. G. Kevrekidis, J. Opt. **15**, 044013 (2013).

[33] T. Penati, M. Sansottera, S. Paleari, V. Koukouloyannis, and P. G. Kevrekidis, Physica D **370**, 1 (2018).

[34] M. Öster, M. Johansson, and A. Eriksson, Phys. Rev. E **67**, 056606 (2003).

[35] L. Q. English, F. Palmero, P. Candiani, J. Cuevas, R. Carretero-González, P. G. Kevrekidis, and A. J. Sievers, Phys. Rev. Lett. **108**, 084101 (2012).

[36] S. R. Bickham, S. A. Kiselev, and A. J. Sievers, Phys. Rev. B **47**, 14206 (1993).

[37] F. Palmero, L. Q. English, J. Cuevas, R. Carretero-González, and P. G. Kevrekidis, Phys. Rev. E **84**, 026605 (2011).